Unsteady pylon loading caused by propeller-slipstream impingement for tip-mounted propellers

Sinnige, Tomas; De Vries, Reynard; Della Corte, Biagio; Avallone, Francesco; Ragni, Daniele; Eitelberg, Georg; Veldhuis, Leo L.M.

DOI
10.2514/1.C034696

Publication date
2018

Document Version
Final published version

Published in
Journal of Aircraft

Citation (APA)
Sinnige, T., De Vries, R., Della Corte, B., Avallone, F., Ragni, D., Eitelberg, G., & Veldhuis, L. L. M. (2018). Unsteady pylon loading caused by propeller-slipstream impingement for tip-mounted propellers. *Journal of Aircraft*, *55*(4), 1605-1618. https://doi.org/10.2514/1.C034696

JOURNAL OF AIRCRAFT
Vol. 55, No. 4, July–August 2018

Unsteady Pylon Loading Caused by Propeller-Slipstream Impingement for Tip-Mounted Propellers

Tomas Sinnige* and Reynard de Vries†
Delft University of Technology, 2629 HS Delft, The Netherlands
Biagio Della Corte‡
University of Naples Federico II, 80138 Naples, Italy
and
Francesco Avallone,§ Daniele Ragni,¶ Georg Eitelberg,** and Leo L. M. Veldhuis**
Delft University of Technology, 2629 HS Delft, The Netherlands

DOI: 10.2514/1.C034696

An experimental analysis was performed of the unsteady aerodynamic loading caused by the impingement of a propeller slipstream on a downstream lifting surface. When installed on an aircraft, this unsteady loading results in vibrations that are transmitted to the fuselage and are perceived inside the cabin as structure-borne noise. A pylon-mounted tractor–propeller configuration was installed in a low-speed wind tunnel at Delft University of Technology. Surface-microphone and particle-image-velocimetry measurements were taken to quantify the pressure fluctuations on the pylon and visualize the impingement phenomena. It was confirmed that the propeller tip vortex is the dominant source of pressure fluctuations on the pylon. Along the path of the tip vortex on the pylon, a periodic pressure response occurs with strong harmonics. The amplitude of the pressure fluctuations increases with increasing thrust setting, whereas the unsteady lift coefficient displays a nonmonotonic dependency on the propeller thrust. The lowest integral unsteady loads were obtained for cases with approximately integer ratios between the pylon chord and the wavelength of the perturbation associated with the propeller tip vortices. This implies that structure-borne-noise reductions might be obtained by matching the pylon chord with an integer multiple of the axial separation between the propeller tip vortices.

Nomenclature

BPF	=	blade-passage frequency, Hz
c	=	pylon chord, m
C'_L	=	unsteady lift coefficient
$C'_{L_{\text{rms}}}$	=	rms of unsteady lift coefficient [Eq. (2)]
C'_p	=	p'/q_∞, unsteady pressure coefficient
$\tilde{C}'_p$	=	Fourier coefficients of unsteady pressure coefficient
$C'_{p_{\text{adv}}}$	=	unsteady pressure coefficient on advancing side of the pylon
$C'_{p_{\text{retr}}}$	=	unsteady pressure coefficient on retreating side of the pylon
$C'_{p_{\text{rms}}}$	=	rms of unsteady pressure coefficient
$\overline{C'_{p_{\text{rms}}}}$	=	spatial average of rms of unsteady pressure coefficient [Eq. (1)]
C_T	=	$T/\rho_\infty n^2 D^4$, propeller thrust coefficient
c_{b}	=	blade chord, m
c_{s}	=	sleeve chord, m
D	=	propeller diameter, m
f	=	frequency, Hz
J	=	V_∞/nD, propeller advance ratio
n	=	propeller rotational speed, Hz
p'	=	unsteady pressure, Pa
q_∞	=	freestream dynamic pressure, Pa
R	=	propeller radius, m
r	=	radial coordinate, m
T	=	propeller thrust, N
t	=	time, s
$\lvert\mathbf{V}\rvert$	=	$\sqrt{V_X^2 + V_Y^2}$, in-plane velocity magnitude, m/s
$\lvert\overline{\mathbf{V}^{\text{prop-off}}}\rvert$	=	time-averaged in-plane velocity magnitude with propeller off, m/s
$\lvert\mathbf{V}^{\text{prop-on}}\rvert$	=	in-plane velocity magnitude with propeller on, m/s
V_{disk}	=	equivalent velocity at propeller disk, m/s
V_X	=	axial velocity, m/s
$V_X^{\text{prop-on}}$	=	axial velocity with propeller on, m/s
V_Y	=	lateral velocity, m/s
V_∞	=	freestream velocity, m/s
X	=	axial coordinate from propeller center, m
X_{pyl}	=	axial coordinate from pylon leading edge, m
X_{s}	=	axial coordinate from sleeve leading edge, m
Y	=	lateral coordinate from propeller center, m
Z	=	vertical coordinate from propeller center (spanwise direction), m
Z_{max}	=	spanwise coordinate of upper integration limit in Eqs. (1) and (2), m
Z_{min}	=	spanwise coordinate of lower integration limit in Eqs. (1) and (2), m
α	=	angle of attack, deg
β	=	blade pitch angle, deg
Γ	=	circulation, m^2/s
$\Delta C'_p$	=	difference between unsteady pressure coefficients on retreating and advancing sides of the pylon
$\lvert\Delta\mathbf{V}\rvert$	=	in-plane velocity magnitude induced by propeller, m/s

Presented as Paper 2017-1175 at the 55th AIAA Aerospace Sciences Meeting, Grapevine, TX, 9–13 January 2017; received 7 August 2017; revision received 19 November 2017; accepted for publication 22 November 2017; published online 3 January 2018.

*Ph.D. Candidate, Flight Performance and Propulsion Section, Faculty of Aerospace Engineering, Kluyverweg 1; T.Sinnige@tudelft.nl. Member AIAA.
†M.Sc. Student, Flight Performance and Propulsion Section, Faculty of Aerospace Engineering, Kluyverweg 1. Member AIAA.
‡M.Sc. Student, Faculty of Aerospace Engineering, Corso Umberto I 40.
§Postdoctoral Researcher, Aeroacoustics Section, Faculty of Aerospace Engineering, Kluyverweg 1. Member AIAA.
¶Assistant Professor, Aeroacoustics Section, Faculty of Aerospace Engineering, Kluyverweg 1. Member AIAA.
**Professor, Flight Performance and Propulsion Section, Faculty of Aerospace Engineering, Kluyverweg 1. Member AIAA.

ΔV_X = axial velocity change due to propeller with respect to freestream, m/s
ΔX = axial separation between propeller center and pylon leading edge, m
ϵ_V = uncertainty of velocity component from particle image velocimetry, m/s
λ = wavelength, m
ρ_∞ = freestream density, kg/m^3
ϕ = blade phase angle, deg
ϕ' = blade phase angle at approximate time of vortex impingement on the pylon leading edge, deg
ω_Z = Z component of vorticity, 1/s
ω_Z^* = $\omega_Z D/V_{\text{disk}}$, Z component of normalized vorticity

I. Introduction

ADVANCES in propeller blade design and a recent focus on hybrid-electric propulsion have revived interest in propeller propulsion systems. Compared to turbofan engines, propellers offer fuel savings of 10–20% [1], at the cost of challenging airframe integration and higher noise levels. To overcome these drawbacks, previous studies [2–5] have proposed an aft-mounted propeller configuration, with dedicated pylons to connect the propellers to the fuselage. Recent work has mostly studied such pylon-mounted propellers in a pusher configuration, but this layout suffers from additional noise generation due to the unsteady interaction of the propeller blades with the pylon wake [6–8]. To avoid such noise penalties, the tractor configuration is favorable. This was confirmed by direct comparisons of the aeroacoustic performance of contra-rotating propellers in semi-installed tractor and pusher configurations [9,10]. In both cases, the propeller noise emissions were found lower for the tractor configuration, especially for cases with relatively low tip speeds and disk loading.

In a tractor-propeller configuration, the pylon is partially immersed in the propeller slipstream. This leads to interaction phenomena comparable to those observed for conventional wing-mounted propellers, which have been studied by multiple researchers [11–16]. The presence of the wing changes the flowfield experienced by the propeller, leading to unsteady blade loads and associated noise and vibrations (upstream effect). At the same time, the increased dynamic pressure and swirl in the propeller slipstream modify the inflow to the wing, affecting its lift distribution (downstream effect). The interaction with the wing causes a marked deformation of the propeller slipstream, as visualized by Felli and Falchi [17] for a marine propeller interacting with a downstream rudder. Apart from the modification of the time-averaged wing loading, the periodic impingement of the wakes and tip vortices of the propeller blades on the wing also results in a time-varying loading component. This loading is periodic at the blade-passage frequency and its harmonics, as shown by the experimental studies by Ljunggren et al. [15] and Johnston and Sullivan [16]. The locally increased turbulence levels in the slipstream [18] will also lead to periodic laminar-to-turbulent transition on the downstream element [19,20], introducing additional load fluctuations. This secondary phenomenon is not considered in the current paper.

The unsteady loading caused by the impingement of the propeller slipstream on the wing or pylon results in structural vibrations, which are transmitted to the fuselage [21]. These vibrations are then perceived as additional noise inside the cabin, reducing passenger comfort. This phenomenon is known as structure-borne noise and has been extensively investigated in the 1980s, both experimentally [22–26] and analytically [27–31]. Its relevance was first outlined by the study of Miller et al. [22], who identified the propeller blade-tip vortices as dominant sources of pressure fluctuations on the wing. The amplitude of these hydrodynamic pressure fluctuations was found to be about 15 dB higher than the acoustic pressure measured at the wind-tunnel ceiling, representative of the fuselage sidewall location [22]. This shows that the unsteady pressures caused by the impingement of the propeller slipstream can be an important source of cabin noise. A secondary source of structure-borne noise can be caused by unsteady loading on the propeller blades [21,31]. However, the contribution due to the propeller-slipstream impingement on the wing or pylon is considered dominant [21,23,28].

The potential impact on passenger comfort of the unsteady loads caused by propeller-slipstream impingement motivates the need to understand the mechanism by which these loads are generated. However, thus far, limited information is available regarding the spatial distribution of the pressure fluctuations. Also, the sensitivity to operating conditions such as thrust setting, propeller–pylon spacing, and angle of attack has not been treated in detail. The current paper presents an experimental study that combined unsteady surface-pressure measurements at the pylon with flowfield visualizations using particle image velocimetry (PIV). In this way, the unsteady interaction effects caused by the impingement of the propeller slipstream are quantified and explained for a typical pylon-mounted tractor-propeller configuration. The focus of the paper is on the aerodynamic forcing function of the structure-borne noise; the structural response of the pylon to this forcing function is not considered. This also implies that fluid–structure interaction is not taken into account. A single-rotating propeller was used to allow for a clear interpretation of the unsteady loading on the pylon, caused by the unsteady flow structures in the propeller slipstream. Similar interaction effects will occur for contra-rotating propellers, although the flowfield in the slipstream of such propellers is more complex due to interactions between the wakes and tip vortices shed from both blade rows, and thus the unsteady loading on the pylon will most likely feature a more complicated spatial and temporal behavior. Note that, from an aerodynamic point of view, the considered pylon-mounted layout is equivalent to a wing-tip-mounted configuration, which provides additional aerodynamic benefits due to improved tip-vortex recovery [32,33]. Moreover, the work is also relevant for conventional wing-mounted propellers, for which the unsteady interaction effects will be comparable.

II. Experimental Setup

A. Wind-Tunnel Facility and Models

Experiments were performed at the low-turbulence tunnel at Delft University of Technology. This low-speed, closed-circuit wind tunnel features a test section of 1.80×1.25 m, with a maximum flow velocity of 120 m/s and a freestream turbulence level below 0.1%. A typical pylon-mounted tractor-propeller configuration was simulated by positioning a sting-mounted propeller upstream of a generic pylon model. A photograph of the test setup with the propeller installed in the test section is given in Fig. 1, whereas Fig. 2 provides a technical drawing of the setup. Additionally, a CAD model of the setup is attached to this paper as Supplemental Data S1.

The propeller model had a diameter of 0.237 m, with four straight blades set to a pitch angle of 23.9 deg at 75% of the radius (defined between the local chord line and the propeller plane). A technical drawing of the propeller geometry, including blade sections at eight radial stations, is shown in Fig. 3. In addition, Fig. 4 provides the radial distributions of the blade chord and the pitch angle. The propeller was

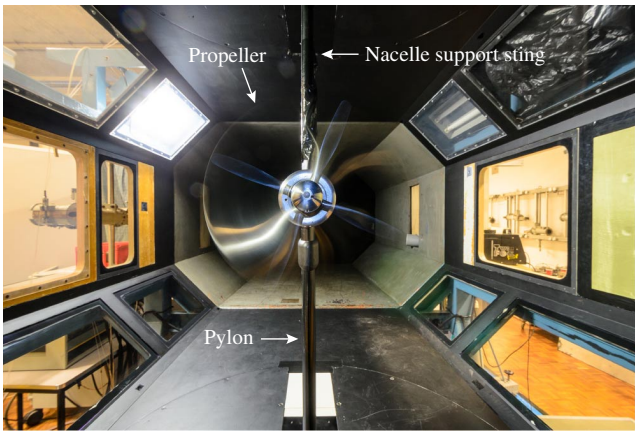

Fig. 1 Propeller–pylon test setup installed in the low-turbulence tunnel at Delft University of Technology.

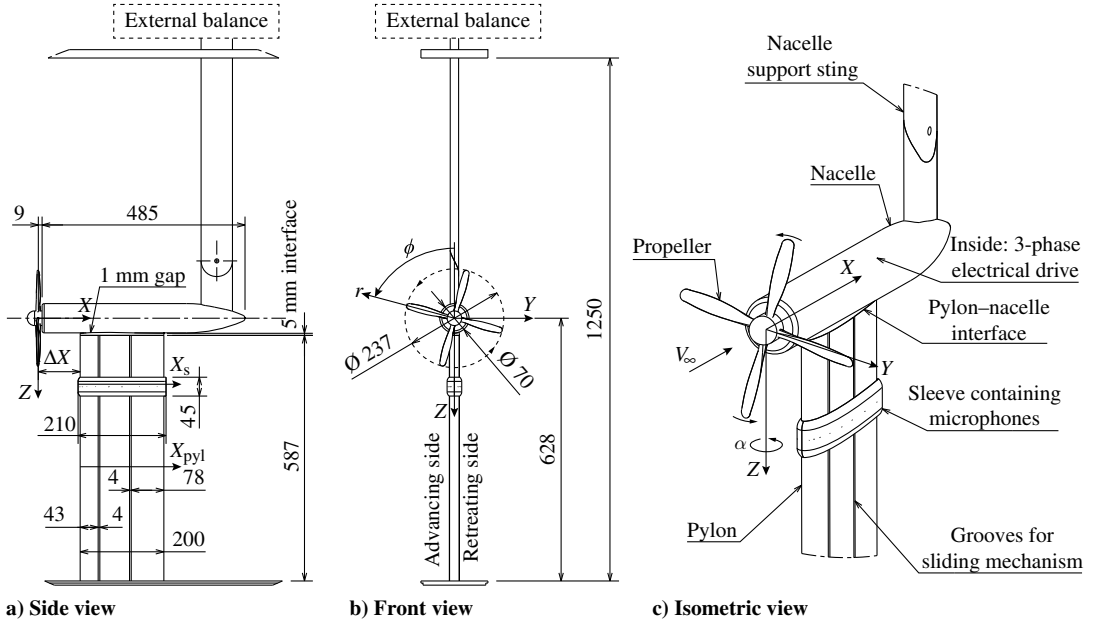

Fig. 2 Technical drawing of the propeller–pylon test setup; dimensional numbers in millimeters.

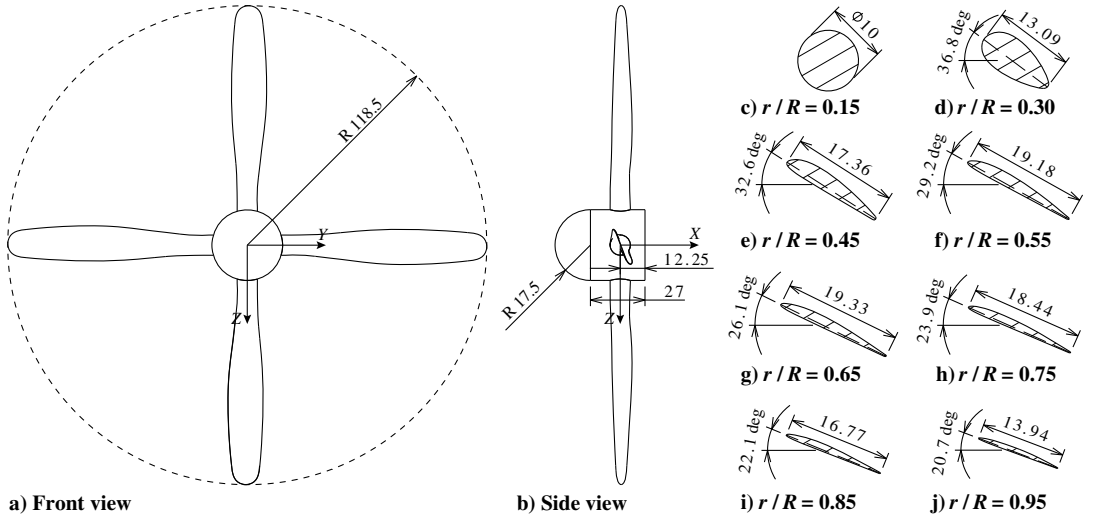

Fig. 3 Technical drawing of the propeller geometry; dimensional numbers in millimeters.

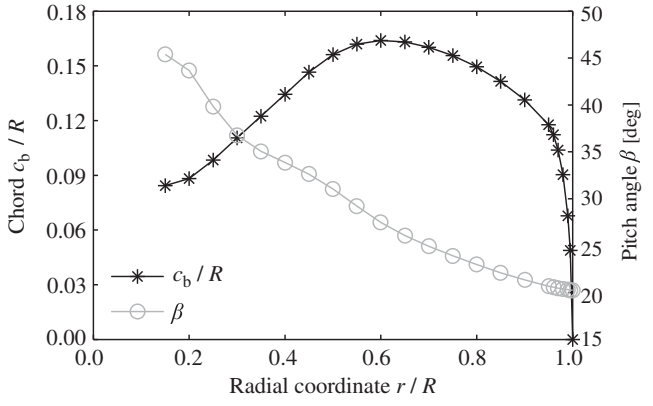

Fig. 4 Radial distributions of the propeller blade chord and pitch angle.

driven by an electrical motor, housed inside a 70-mm-diam nacelle. This nacelle was connected to an external six-component balance via a support sting.

The pylon model featured a NACA 0012 profile with a chord of 0.200 m and a span of 0.592 m. In this way, the propeller could be positioned in the center of the test section with the pylon mounted to the floor of the wind tunnel. A gap of 1 mm was left between the nacelle and the pylon. This allowed for external balance measurements of the propeller forces with and without pylon installed and prevented the transmission of potential vibrations caused by the propeller to the pylon. The pylon was equipped with a sleeve containing 16 microphones aligned in the streamwise direction, as discussed in more detail in Sec. II.D. The sleeve had a width of 0.045 m and a thickness of 0.005 m, whereas the shape was designed as an offset from the pylon's baseline NACA 0012 profile, resulting in a chord of $c_s = 0.210$ m. Quantitative flowfield measurements using PIV showed that the presence of the sleeve did not significantly alter the flowfield compared to that around a two-dimensional pylon with the cross section of the sleeve. The sleeve was traversed in the vertical direction (pylon spanwise direction) through two grooves on each side of the pylon, centered at $X_{pyl}/c = 0.23$ and $X_{pyl}/c = 0.60$ from the leading edge. An equivalent pylon model without grooves was used for the flowfield measurements with PIV.

B. Propeller Performance Measurements

The thrust of the propeller was measured using an external six-component balance. Both the configurations with and without the pylon installed were considered. In this way, the impact of the installation of the

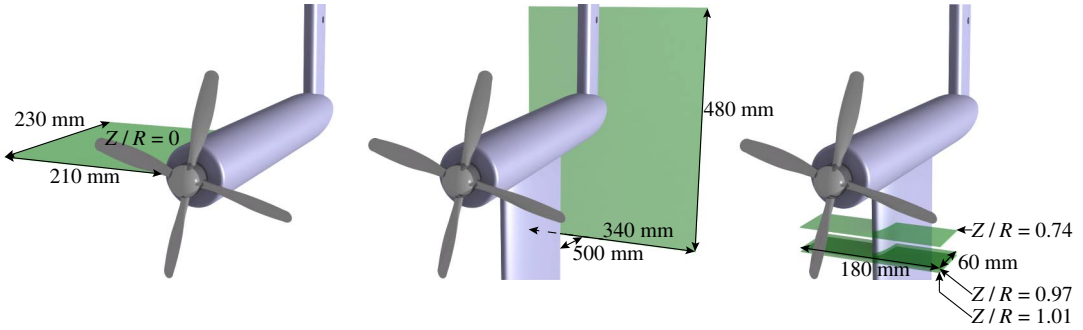

a) Isolated slipstream (SSFOV) **b) Slipstream deformation (WFOV)** **c) Slipstream impingement (LEFOV)**

Fig. 5 Illustration of the PIV setups.

pylon on the propeller performance could be measured. Tare measurements were performed with the blades removed to subtract the drag contributions of the nacelle and support sting. The change in drag of the nacelle and support sting due to the increased dynamic pressure and swirl in the propeller slipstream was not corrected for. Evaluations of the results from repeated measurements showed that the thrust data were reproducible to within approximately 2%.

C. Flowfield Measurements

Flowfield measurements were taken with PIV. Three different setups were used to characterize the flowfield in the slipstream of the isolated propeller (SSFOV), the propeller-slipstream deformation caused by the pylon (WFOV), and the slipstream-impingement process at the pylon leading edge (LEFOV). The corresponding measurement setups are illustrated in Fig. 5. Table 1 provides detailed imaging and data-acquisition characteristics for each setup. In all cases, postprocessing of the particle images was performed using an iterative multigrid approach [34]. Furthermore, the uncertainty of the velocity measurements was estimated taking into account the finite accuracy of the cross correlation, the finite number of samples used for averaging, and image disparity between the two cameras for the stereoscopic setups.

1. Isolated Propeller Slipstream (SSFOV)

The flowfield downstream of the isolated propeller (without pylon) was measured using stereoscopic PIV (Fig. 5a). Ignoring the influence of the support sting, which was placed sufficiently far downstream of the propeller plane to have a negligible effect on the propeller loading, the isolated propeller case is axisymmetric. Therefore, the complete slipstream could be mapped using measurements in a single plane positioned at the vertical position of the propeller axis ($Z/R = 0$). To clearly identify the characteristics of the blade wakes and tip vortices, the measurements were taken phase-locked with the propeller blade position. This was achieved using an optical one-per-revolution trigger signal integrated into the motor driving the propeller. Moreover, phase-uncorrelated measurements were performed to obtain a representation of the time-averaged flowfield in the propeller slipstream.

2. Propeller-Slipstream Deformation Caused by the Pylon (WFOV)

The deformation of the propeller slipstream due to the interaction with the pylon was evaluated using a stereoscopic PIV setup with the field of view positioned at 2.5 times the chord length downstream of the pylon trailing edge (Fig. 5b). Two measurement planes were used, after which the data were combined in postprocessing to obtain the final results. Measurements were taken both with and without the pylon, while only phase-uncorrelated acquisitions were performed. The microphone sleeve was not present during these measurements, and the pylon model without grooves was used.

3. Propeller-Slipstream Impingement at the Pylon Leading Edge (LEFOV)

The impingement of the blade wakes and tip vortices at the leading edge of the pylon was visualized with a planar PIV setup (Fig. 5c). Illumination was provided on each side of the pylon by simultaneously using two lasers. Two cameras were employed, with each camera providing a field of view on each side of the pylon. The resulting vector fields from both cameras were combined to obtain the final measurement data, centered around the leading edge of the pylon. Measurements were taken at three vertical positions, corresponding to spanwise locations in the blade-wake impingement region ($Z/R = 0.74$) and surrounding the tip-vortex impingement region ($Z/R = 0.97$ and $Z/R = 1.01$). Phase-uncorrelated data were acquired to confirm the expected steady-state interaction effects. Moreover, phase-locked measurements displayed the development of the blade wakes and tip vortices during the impingement process. The approximate phase angle at which the tip vortex impinged on the leading edge of the pylon was defined here as a phase angle of $\phi' = 0$ deg, while additional measurements were taken at phase angles of −17.5, −2.5, 5, 27.5, and 52.5 deg. Again, the microphone

Table 1 PIV imaging and data-acquisition characteristics

	SSFOV	WFOV	LEFOV
PIV setup	Stereoscopic	Stereoscopic	Planar
Laser	1 × Nd:YAG 200 mJ laser		2 × Nd:YAG 200 mJ laser
Cameras	2 × 16 Mpixel CCD image sensor, 7.4 × 7.4 μm/pixel		
Objective	200 mm $f/4$		
Field-of-view size, mm	210 × 230	340 × 480	180 × 60
Field-of-view position	$Z/R = 0$	$X_{pyl} = 3.5c$	$Z/R = [0.74, 0.97, 1.01]$
Pulse separation, μs	20	40	5
Maximum particle displacement, pixel	14	13	10
Digital resolution, pixel/mm	18	8	50
Image pairs phase-locked	250	N/A	300
Image pairs uncorrelated	500	500	500
Interrogation window size, pixel	12 × 12	32 × 32	24 × 24
Window overlap factor, %	75	50	50
Vector spacing, mm	0.2	2.0	0.2
Uncertainty ϵ_V/V_∞	0.016	0.016	0.012

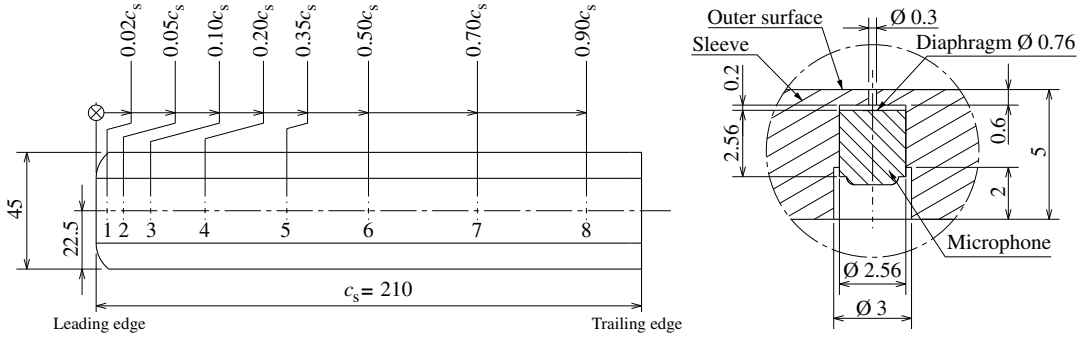

a) Side view **b) Cross-sectional view at microphone location**

Fig. 6 Technical drawing of the microphone sleeve; dimensional numbers in millimeters.

sleeve was removed for these measurements, and the pylon model without grooves was used.

D. Surface-Pressure Measurements

The unsteady loading on the pylon was quantified using flush-mounted microphones integrated into the sleeve discussed in Sec. II.A. On each side of the sleeve, eight Sonion 8010T microphones were installed, at (linear) distances from the leading edge of the sleeve of 0.02, 0.05, 0.10, 0.20, 0.35, 0.50, 0.70, and 0.90 times the sleeve chord (Fig. 6a). The microphones were placed recessed from the surface in individual cavities (Fig. 6b) with a resonance frequency of approximately 16.8 kHz. No protection grid was installed between the diaphragm of the microphones and the outer flow. The microphones measured in the frequency range of 10 Hz to 11.5 kHz, with a maximum input level of 112 dB at 1 kHz and a noise floor of 28 dBA. A sampling rate of 25.6 kHz was used, with 30 s of acquisition time per data point. Considering the importance of a frequency-dependent calibration [15], such a calibration was performed using an external reference microphone with a known frequency response. Phase-locking was applied during postprocessing to extract the periodic signal directly related to the propeller-slipstream impingement phenomena. The measurement data were divided into individual rotations using a simultaneously recorded optical one-per-revolution trigger signal and subsequently averaged per phase angle. In this way, the parts of the signal that were not related to the periodic slipstream-impingement phenomena were eliminated.

E. Structure-Borne-Noise Indicators

When mounted on the fuselage of an aircraft, the pressure fluctuations on the pylon introduce vibrations into the airframe, which are perceived as noise inside the cabin. The study presented in this paper only focuses on the aerodynamic forcing function causing the structure-borne noise. Therefore, the actual characteristics of the structure are not considered, and the exact structure-borne noise levels cannot be predicted. To relate the unsteady pressures measured on the pylon to their potential impact on structure-borne noise generation without consideration of the structural characteristics, two structure-borne-noise indicators were defined. These could then be used to compare the results measured at the different operating conditions in terms of their importance for structure-borne noise.

1. *Average Root Mean Square of the Pressure Fluctuations*

The amplitude of the pressure fluctuations on the pylon surface is representative of the total energy available for structure-borne noise generation. Therefore, the first structure-borne-noise indicator was defined as the spatial average of the rms of the pressure fluctuations over the pylon surface:

$$\overline{C'_{p_{\mathrm{rms}}}} = \frac{1}{2c(Z_{\max}-Z_{\min})}\int_{Z_{\min}}^{Z_{\max}}\int_0^c\left(\sqrt{\frac{1}{2\pi}\int_0^{2\pi} C'_{p_{\mathrm{adv}}}(X_{\mathrm{pyl}},Z,\phi)^2\,\mathrm{d}\phi} + \sqrt{\frac{1}{2\pi}\int_0^{2\pi} C'_{p_{\mathrm{retr}}}(X_{\mathrm{pyl}},Z,\phi)^2\,\mathrm{d}\phi}\right)\mathrm{d}X_{\mathrm{pyl}}\,\mathrm{d}Z \quad (1)$$

The lower integration limit $Z_{\min}$ was set to the first data point along the pylon span ($Z/R = 0.54$), whereas the upper limit $Z_{\max}$ was set as low as possible without excluding part of the slipstream for any of the measurement cases ($Z/R = 1.25$). The pressure parameter defined by Eq. (1) is representative of the structure-borne noise levels only if all vibrational energy is transmitted into the structure; i.e., the structural displacement at each location is assumed to be in phase with the aerodynamic loading acting on it.

2. *Unsteady Lift Coefficient*

Although the average pressure-fluctuation level defined by Eq. (1) is representative of the total energy available for structure-borne noise generation, it is not necessarily directly related to the actual structure-borne noise levels because of the assumption that the structural displacement is in phase with the aerodynamic excitation at each location on the pylon. In a more realistic scenario, the relative phases of the pressure fluctuations at each location on the pylon affect the total unsteady loading. Assuming that the pylon is an elastic body with infinitely high speed of sound, all input loads are instantaneously transmitted to the fuselage. In such case, the unsteady lift coefficient, obtained from integration of the measured pressure fluctuations, is representative of the level of structure-borne noise:

$$C'_{L_{\mathrm{rms}}} = \frac{1}{c(Z_{\max}-Z_{\min})} \cdot \sqrt{\frac{1}{2\pi}\int_0^{2\pi}\left(\int_{Z_{\min}}^{Z_{\max}}\int_0^c \Delta C'_p(X_{\mathrm{pyl}},Z,\phi)\,\mathrm{d}X_{\mathrm{pyl}}\,\mathrm{d}Z\right)^2\mathrm{d}\phi} \quad (2)$$

where $\Delta C'_p = (C'_{p_{\mathrm{retr}}} - C'_{p_{\mathrm{adv}}})$ is the difference between the unsteady pressure coefficient across the pylon. The same integration limits were used as for Eq. (1).

To allow for the computation of the integral time-dependent loading on the pylon using Eq. (2), the spacing between adjacent measurement locations needs to be smaller than the characteristic wavelength of the periodic perturbation. If this is not the case, the relevant flow features that are convecting downstream over the pylon chord will temporarily disappear from the data set when they are positioned between two adjacent microphones. This would lead to an incorrect measurement of the time-dependent loading. At the baseline operating condition, the axial separation between consecutive blade wakes in the propeller slipstream was around 47 mm. Therefore, the chordwise density of integration points was increased. This was done by interpolating the pressure waveforms between each pair of adjacent microphones (in the chordwise direction) in both space and time. The procedure is illustrated in Fig. 7, in which two measurement locations are indicated by the subscripts 1 and 2, and an interpolated point is identified by the subscript i. Assuming a linear pressure evolution between the measurement locations and a constant phase velocity, the amplitude of the unsteady pressure at the interpolated point can be computed once the phase difference between measurement points 1 and 2 is known. This phase difference is directly related to the phase velocity, which was computed from the derivative of the cross-spectral density function of the raw pressure signals of the two microphones considered, following

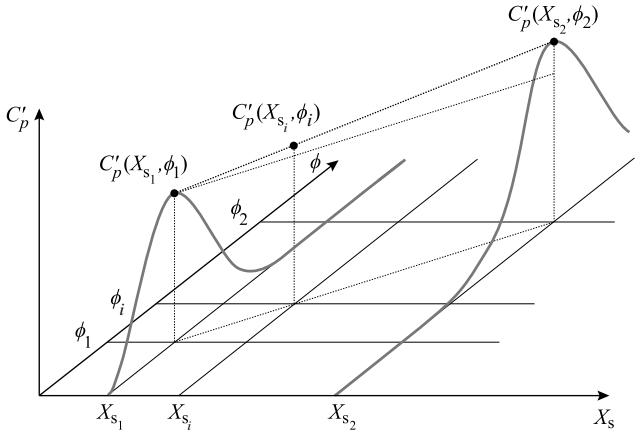

Fig. 7 Illustration of the microphone interpolation procedure.

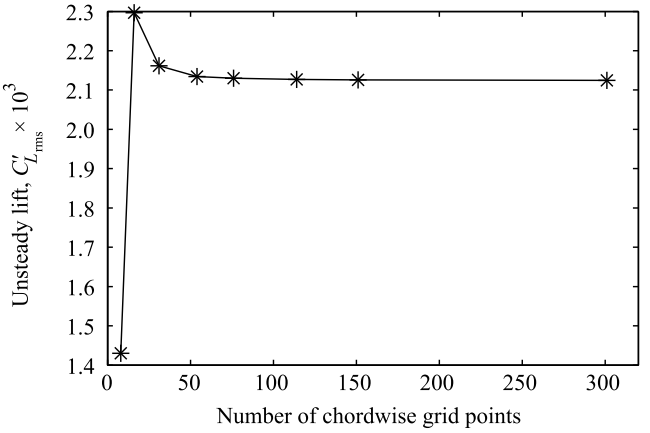

Fig. 8 Sensitivity of unsteady lift coefficient to number of chordwise grid points used in microphone interpolation procedure.

the approach introduced in [35]. On the spanwise part of the pylon not immersed in the slipstream, the prediction of the phase velocity was complicated by the absence of clearly defined flow structures. The resulting noise in the interpolated results was verified not to impact the computed unsteady loading because that was dominated by the strong pressure fluctuations caused by the blade wakes and tip vortices.

The sensitivity of the interpolation procedure to the number of chordwise grid points was investigated by computing the unsteady lift coefficient from Eq. (2) for a number of different grid densities, as shown in Fig. 8. Note that the case with eight chordwise points corresponds to the original microphone density, without interpolation. It can be seen that the interpolation procedure converges toward an asymptotic value for high grid densities. Based on these results, a total number of grid points of 76 was selected as a compromise between accuracy and required processing time. At this grid density, the unsteady lift coefficient was within 0.2% of the value obtained at the finest grid spacing considered. The need for the interpolation scheme is confirmed by observing that the unsteady lift coefficient computed without interpolation (eight grid points) differs about 30% from the asymptotic value.

F. Description of Analyzed Test Cases

The propeller performance measurements and flowfield visualizations using PIV were acquired at a freestream velocity of 40 m/s. All microphone measurements, on the other hand, were performed at a freestream velocity of $V_\infty = 10$ m/s to maximize the dynamic range of the microphone data. Analysis of a number of PIV measurements taken at 10 m/s showed that the difference in freestream velocity between the PIV and microphone measurements did not appreciably affect the dominant flow phenomena. The effects of propeller thrust setting, propeller–pylon spacing, and angular inflow were investigated by taking measurements for a range of propeller advance ratios, axial separations between propeller and pylon, and angles of attack. A baseline advance ratio of $J = 0.8$ was selected, which represented an intermediate blade loading condition at which the propeller featured a linear response of the thrust coefficient. The corresponding value of the thrust coefficient C_T equaled 0.095. In addition, advance ratios of 0.7, 0.9, and 1.0 were considered to assess the sensitivity of the unsteady pylon loads to the thrust setting. The propeller–pylon spacing ΔX was varied from 0.21 up to 0.84 times the propeller diameter, at a baseline spacing of $0.42D$. Finally, the angle of attack was changed from 0 up to 12 deg at 6 deg intervals, and measurements were also taken at −6 deg to obtain insight into the effect of the propeller rotation direction on the unsteady loads. All results presented in this paper were obtained for the baseline operating conditions ($J = 0.8$, $\Delta X = 0.42D$, $\alpha = 0$ deg), unless mentioned otherwise.

III. Results

A. Propeller Performance

The impact of the downstream pylon on the propeller thrust was evaluated using an external balance. Figure 9 shows the propeller thrust coefficient as a function of advance ratio for the cases with and without the pylon installed. The uncertainty of the data was estimated by taking the standard deviation of the thrust coefficients obtained from repeated measurements taken at constant operating conditions. The resulting value is indicated by the error bar displayed in the top left of Fig. 9.

The performance of the isolated propeller (pylon-off) presented in Fig. 9 follows the expected trend. The thrust increases with decreasing advance ratio, with a nonlinear response observed at the lowest advance ratio considered ($J = 0.7$). The presence of the downstream pylon causes blockage and upwash, introducing asymmetric inflow conditions comparable to those experienced when operating the propeller at nonzero angle of attack. As a result, the time-averaged thrust of the propeller is expected to increase slightly [11]. As shown in Fig. 9, the measured propeller thrust was hardly affected by the installation of the pylon. An increase in thrust of about 1% was observed with the pylon installed, which was within the reproducibility of the balance measurements. The asymmetric inflow conditions caused by the installation of the pylon might have resulted in nonnegligible unsteady loading on the propeller blades [36]. However, this time-dependent blade loading could not be measured in the used test setup. The magnitude of the upstream effect will increase when the pylon is loaded or when the propeller–pylon spacing is decreased.

B. Propeller Slipstream Flowfield

The flowfield in the slipstream of the isolated propeller was measured using stereoscopic PIV (SSFOV setup, Fig. 5a), phase-locked with the propeller blade position. Figure 10 presents the resulting contours of the axial velocity. To highlight the velocities

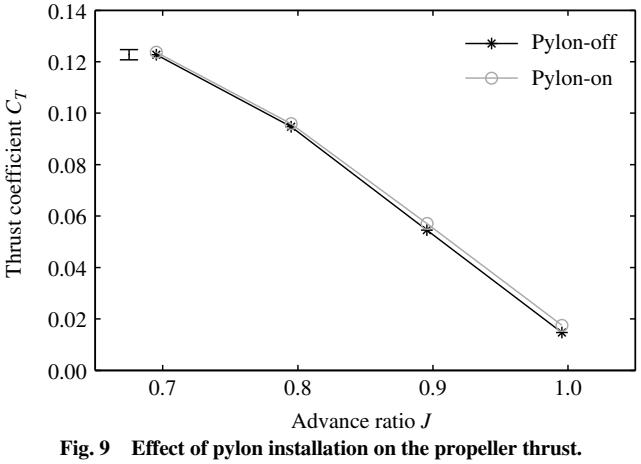

Fig. 9 Effect of pylon installation on the propeller thrust.

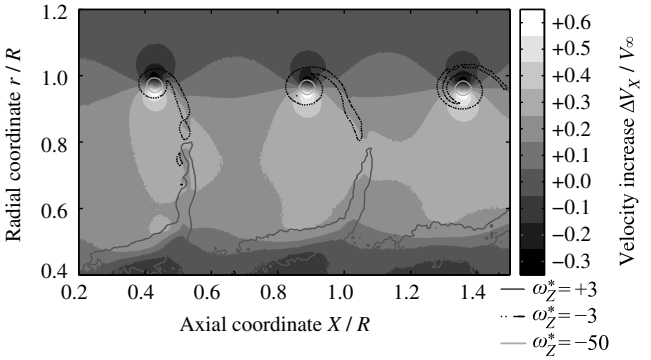

Fig. 10 Phase-locked axial velocity variation in the slipstream of the isolated propeller, with contours of constant normalized vorticity superimposed.

induced by the slipstream, the velocity field is presented as an offset from the freestream velocity ($\Delta V_X = V_X^{\text{prop-on}} - V_\infty$). Contour lines of constant normalized vorticity $\omega_Z^* = \omega_Z D/V_{\text{disk}}$ are included in Fig. 10, where ω_Z is the Z component of the vorticity, and V_{disk} is the equivalent velocity at the propeller disk estimated from actuator-disk theory [11].

The axial velocity difference plot shown in Fig. 10 highlights several important characteristics of the propeller slipstream. The axial velocity is increased within the slipstream, corresponding to a positive thrust generated by the propeller. Within the streamtube, three distinct flow structures are visible, associated with each blade passage. At the most inboard radial stations ($r/R < 0.5$), the propeller root vortex can be seen. Moving outboard ($0.5 < r/R < 1.0$), the blade wakes are present. In the initial part of the slipstream ($X/R < 0.5$), these wakes are practically straight. However, the nonuniform distribution of axial velocity in the propeller slipstream causes the shape of the blade wakes to become increasingly crescent when convecting downstream. A change in sign of normalized vorticity occurred in the blade wake around $r/R = 0.8$. This corresponds to the radial position of maximum loading on the propeller blades. Finally, the blade-tip vortices cause strong velocity fluctuations around the edge of the slipstream ($r/R \approx 1.0$).

C. Propeller-Slipstream Deformation Caused by the Pylon

To assess the effect of installation of the pylon on the propeller slipstream, the PIV measurements in the wake of the models are considered (WFOV setup, Fig. 5b). Figure 11 provides the velocity fields for the configurations with and without the pylon installed. Additionally, a reference case is included for which both the propeller blades and the pylon were removed (propeller-off, pylon-off), displaying the effect of the support structure on the measured velocity fields. The dashed lines indicate the projections of the nacelle, propeller disk, and pylon on the measurement plane; each subplot only shows those components that were present for that specific configuration.

Figure 11 displays the axial velocity increase due to the thrust-generating propeller and the modification of the propeller slipstream due to the installation of the pylon. For all configurations, the nacelle caused a strong velocity deficit around the propeller center. Moreover, a decrease in axial velocity can be seen in the middle of the upper half of the field of view ($Y/R = 0, Z/R < 0$). This was caused by the support sting to which the propeller was connected (Figs. 1 and 2). This sting was relatively thick, and its aerodynamic characteristics were deteriorated by wiring taped to its backside, resulting in a strong wake velocity deficit (Fig. 11a).

For the isolated propeller (Fig. 11b), the expected axisymmetric velocity distribution was obtained away from the region affected by the presence of the support sting. With the pylon present (Fig. 11c), the velocity deficit in the wake of the pylon is apparent below the propeller disk around $Y/R = 0$. At the location of the measurement plane, the velocity deficit was equal to around 5% of the freestream velocity. Moreover, the propeller slipstream was modified considerably compared to the isolated propeller case. On the advancing side of the pylon ($Y/R < 0$), the slipstream moved away from the propeller axis. On the retreating side ($Y/R > 0$), on the other hand, the slipstream was subjected to a displacement toward the propeller axis. These spanwise displacements of the propeller slipstream on the pylon surface have been discussed previously in literature [11,16,37–39] and are caused by the variations in lift along the pylon span. The swirl and the increased dynamic pressure in the slipstream cause a local increase in lift on the part of the pylon inside the slipstream compared to the part of the pylon outside of the slipstream. The associated spanwise variations in circulation induce a radially inboard-oriented velocity on the retreating side and a radially outboard-oriented velocity on the advancing side. As a consequence, the slipstream is gradually displaced toward the propeller axis on the retreating side and away from the propeller axis on the advancing side. This was confirmed by the surface-pressure measurements taken using the microphones, as discussed in Sec. III.E.

In a realistic operating scenario, the propeller–pylon combination might operate under asymmetric inflow conditions. This leads to a further deformation of the propeller slipstream. Figure 12 displays the flowfields in the wake of the setup for angles of attack of −6, 0, and +6 deg. The results confirm the expected increased strength of the wakes of the pylon and support sting at nonzero angle of attack. Focusing on the slipstream geometries, it is concluded that the deformation of the slipstream is more pronounced at negative angle of attack than at positive angle of attack. This was due to a crossflow component that originated over the nacelle, caused by the pressure difference across the pylon. At negative angle of attack, this crossflow is in the same direction as the induced velocity causing the radially inboard displacement of the slipstream on the retreating side (for an inboard-up rotating propeller). Therefore, the displacement was amplified on the retreating side. At positive angle of attack, on the other hand, the crossflow is oriented in the opposite direction, thereby counteracting the radially inboard displacement of the slipstream on the retreating side. This was confirmed by oil-flow visualizations, as shown in Fig. 13 for the cases at $\alpha = 0$ deg and $\alpha = +6$ deg, and the microphone data. Note that the oil-flow

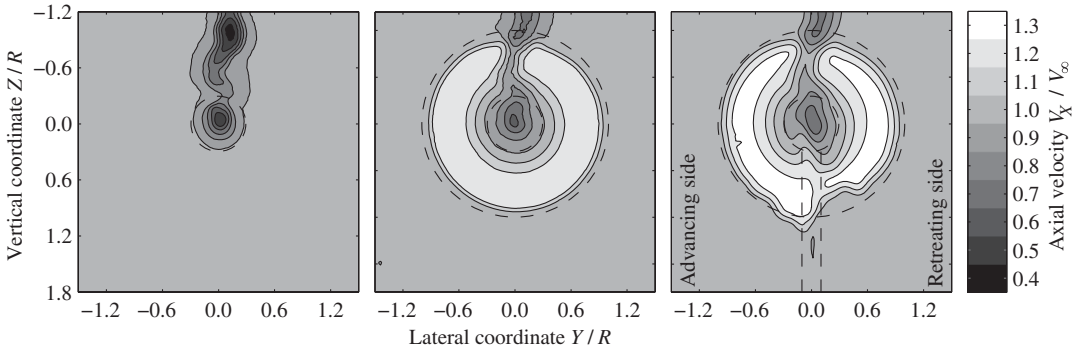

a) Propeller-off, pylon-off **b) Propeller-on, pylon-off** **c) Propeller-on, pylon-on**

Fig. 11 Effect of propeller and pylon installation on the time-averaged slipstream flowfield.

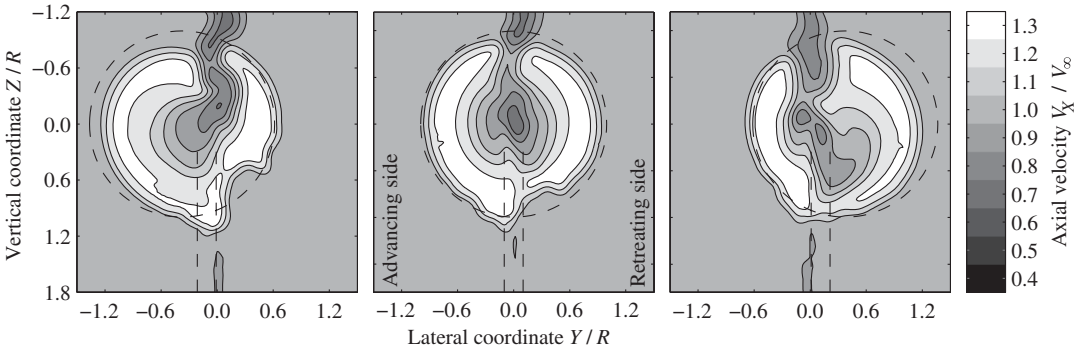

a) $\alpha = -6$ deg **b) $\alpha = 0$ deg** **c) $\alpha = +6$ deg**

Fig. 12 Effect of angle of attack on the time-averaged slipstream flowfield with the pylon installed.

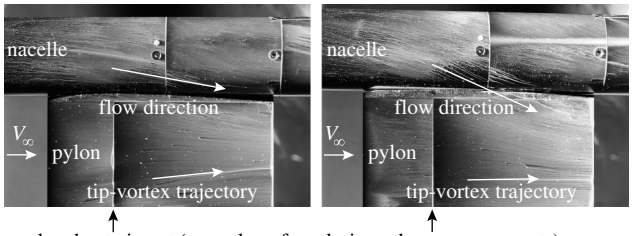

a) $\alpha = 0$ deg **b) $\alpha = +6$ deg**

Fig. 13 Oil-flow visualizations displaying the change in tip-vortex trajectory on the retreating side of the pylon caused by crossflow over the nacelle.

measurements were taken with a slightly modified pylon model, which featured the same dimensions but had a replaceable leading-edge insert mounted flush in the front part of the model. The resulting minor discontinuity in the pylon surface can be recognized in the oil-flow images but is irrelevant for the phenomenon described here.

D. Propeller-Slipstream Impingement at the Pylon Leading Edge

The impingement of the propeller blade wakes and tip vortices on the leading edge of the pylon was visualized using planar PIV (LEFOV setup, Fig. 5c). To ease the interpretation of the results, Fig. 14 displays a schematic representation of the trajectory of a single tip vortex. For clarity, the associated bound and root vortices are omitted. The gray plane represents a measurement plane at an arbitrary position, and the double arrow heads indicate the sign of the

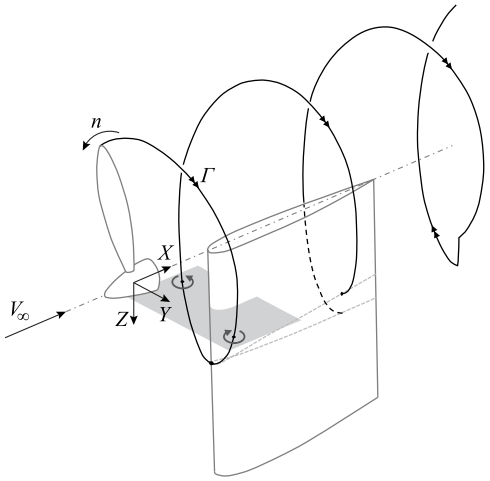

Fig. 14 Illustration of the trajectory of a single tip vortex, and its relation to the measurements using the LEFOV PIV setup.

circulation along the vortex filament. Finally, the gray dotted line on both sides of the pylon represents the path of the tip vortex along the pylon, displaying the spanwise displacement discussed under Fig. 11. It can be seen from Fig. 14 how the velocities induced by the vortex are a function of the position of the vortex relative to the measurement plane. An increase in axial velocity will be induced at the position of the measurement plane if the vortex impinges on the pylon leading edge below the measurement plane, and vice versa.

The blade-wake impingement process was measured at $Z/R = 0.74$ and is displayed in Fig. 15, whereas Fig. 16 shows the data obtained in the tip-vortex plane at $Z/R = 0.97$. In both cases, measurements were taken with and without the propeller blades installed. The difference between the propeller-on and (time-averaged) propeller-off measurements ($|\Delta\mathbf{V}| = |\mathbf{V}^{\text{prop-on}}| - |\overline{\mathbf{V}^{\text{prop-off}}}|$) is considered here to isolate the effect of the propeller on the flowfield. For the results in the wake-impingement region (Fig. 15), contours of normalized vorticity are included to indicate the positions of the blade wakes and tip vortices. The blade position $\phi' = 0$ deg corresponds to the blade phase angle at the approximate time of vortex impingement on the leading edge of the pylon.

The flowfields presented in Fig. 15 clearly display the presence of the blade wakes and tip vortices. Because the measurement plane was positioned below the propeller axis, the lateral distance between the slipstream edges was smaller than the propeller diameter. The increase in velocity in the propeller slipstream can be recognized, with the highest velocities occurring on the retreating side ($Y/R > 0$). This is due to the effective angle of attack perceived by the pylon due to the swirl in the slipstream, causing additional suction on the retreating side. The passage of the blade wake induces an increased suction peak at the leading edge of the pylon on the retreating side (Fig. 15f). This is the result of the modified inflow velocity vector during the wake encounter. The combination of a reduced axial velocity and increased tangential velocity causes a periodic unsteady upwash to the pylon.

Figure 16 displays how the tip vortex approaches the pylon at an oblique angle, caused by the helicoidal trajectory of the vortex (Fig. 16a). Directly before impinging on the leading edge (Fig. 16b), the vortex already bends around the pylon. During impingement (Fig. 16c), the axis of the vortex is nearly tangent to the measurement plane, as can be seen from the very small induced velocities close to the leading edge. On the advancing side ($Y/R < 0$), the pitch angle of the vortex remains similar to that observed before the impingement. The retreating side, on the other hand, displays bending of the vortex due to the acceleration caused by the angle of attack induced by the propwash.

Directly after impingement (Fig. 16d), an increase in axial velocity can be observed near the pylon leading edge, implying that part of the vortex has penetrated the measurement plane. This spanwise displacement of the vortex is due to an image-vortex effect [38–40]. Note that this local displacement near the leading edge is independent of the more gradual spanwise displacement of the tip-vortex trajectory along the chord of the pylon. The latter is caused by the

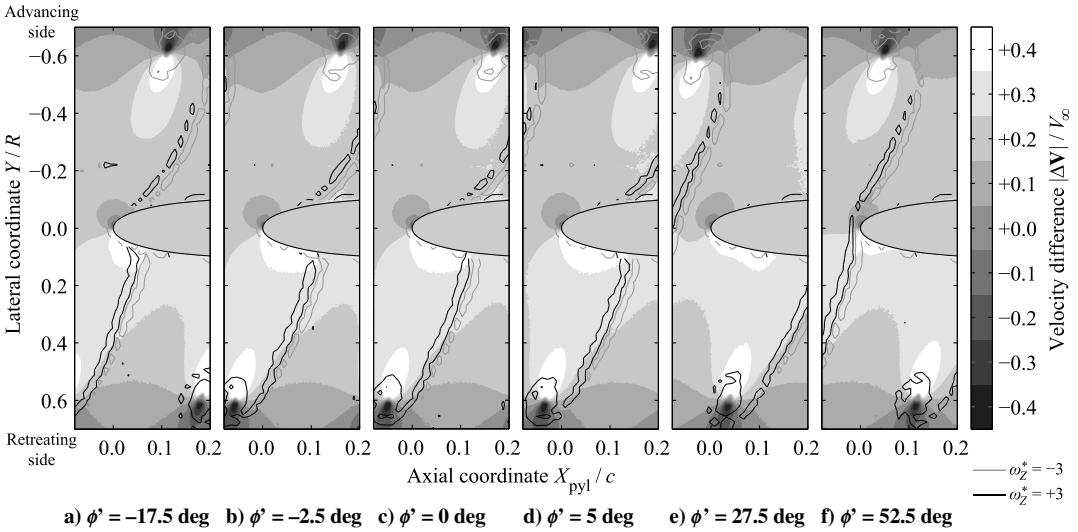

a) ϕ' = –17.5 deg b) ϕ' = –2.5 deg c) ϕ' = 0 deg d) ϕ' = 5 deg e) ϕ' = 27.5 deg f) ϕ' = 52.5 deg

Fig. 15 Wake-impingement process at the pylon leading edge (velocity difference propeller-on minus propeller-off); $Z/R = 0.74$.

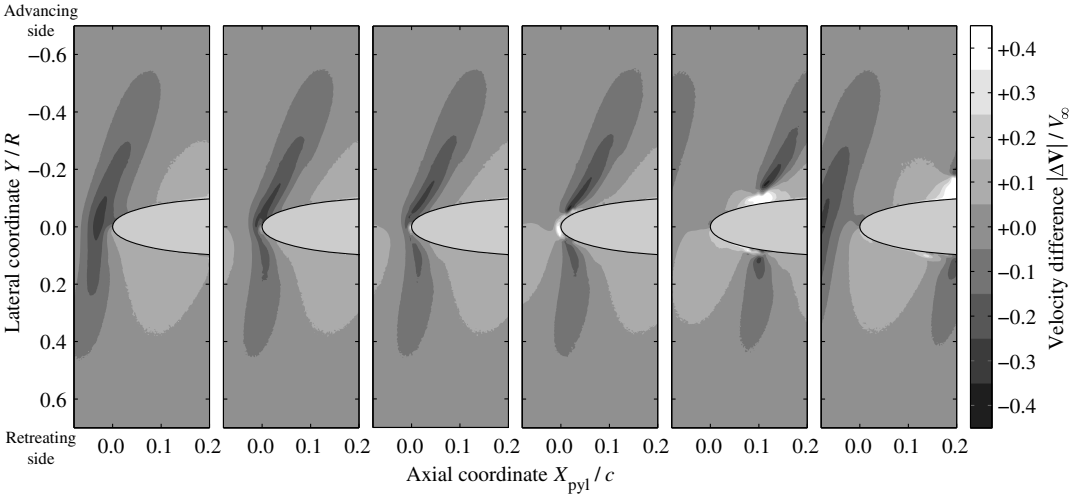

a) ϕ' = –17.5 deg b) ϕ' = –2.5 deg c) ϕ' = 0 deg d) ϕ' = 5 deg e) ϕ' = 27.5 deg f) ϕ' = 52.5 deg

Fig. 16 Vortex-impingement process at the pylon leading edge (velocity difference propeller-on minus propeller-off); $Z/R = 0.97$.

spanwise lift variations across the pylon, as observed in Fig. 11 and highlighted by the microphone results discussed in Sec. III.E.

As the vortex convects downstream (Fig. 16e), it is split. On the retreating side, the vortex segment is almost parallel to the pylon. This can be seen from the fact that the region of influence of the vortex is aligned with the chordwise direction. The velocities induced by the vortex segment on the advancing side are higher than on the retreating side. This is due to the gradual spanwise displacement of the vortex, which makes the vortex penetrate the plane farther on the advancing side than on the retreating side. This spanwise displacement further increases when the vortex continues to convect downstream (Fig. 16f). At this phase angle, the next tip vortex can already be noticed approaching the pylon, stressing the periodic nature of the impingement phenomena.

When the propeller–pylon installation is operated at angle of attack, the impingement phenomena are modified due to the change of the flowfield surrounding the pylon. Figure 17 presents the velocity fields around the pylon leading edge as measured in the tip-vortex impingement plane ($Z/R = 0.97$) at an angle of attack of 6 deg. Again, the results are displayed as the difference between the velocity fields obtained for the propeller-on and propeller-off configurations.

The flowfields provided in Fig. 17 show that the introduction of a positive angle of attack causes increased bending of the vortex on the retreating side. This is due to the increase in velocity over the suction side of the pylon associated with the positive incidence angle. Compared to the symmetric inflow case (Fig. 16), at an angle of attack of 6 deg, the vortex impinges closer to the propeller axis (smaller Z coordinate). This can be seen from the negative velocity induced by the vortex near the pylon leading edge (Fig. 17c) and was expected, considering the slipstream geometries plotted in Fig. 12. After impingement (Figs. 17d–17f), the vortex convects slower on the advancing side than for the case with symmetric inflow. This is due to the locally reduced pylon-induced velocity caused by the positive angle of attack. As a result, at $\alpha = 6$ deg, the vortex is located more upstream at a given phase angle ϕ' compared to the position at $\alpha = 0$ deg. Moreover, on the retreating side, the vortex remains closer to the measurement plane due to the decreased spanwise displacement. The increased shear of the vortex close to the surface leads to additional flow structures, which have been attributed before to the creation of secondary vortices in the chordwise vortex–pylon interaction process [40].

E. Unsteady Pressure Response on the Pylon Surface

The unsteady pressure response on the pylon surface was quantified using the microphones integrated into the sleeve installed around the pylon (Fig. 6). Figure 18 displays the distribution of the rms of the unsteady pressure over the pylon surface, both for the advancing side (Fig. 18a) and the retreating side (Fig. 18b). The black dots indicate the discrete positions at which microphone measurements were taken. The white markers along the dotted lines

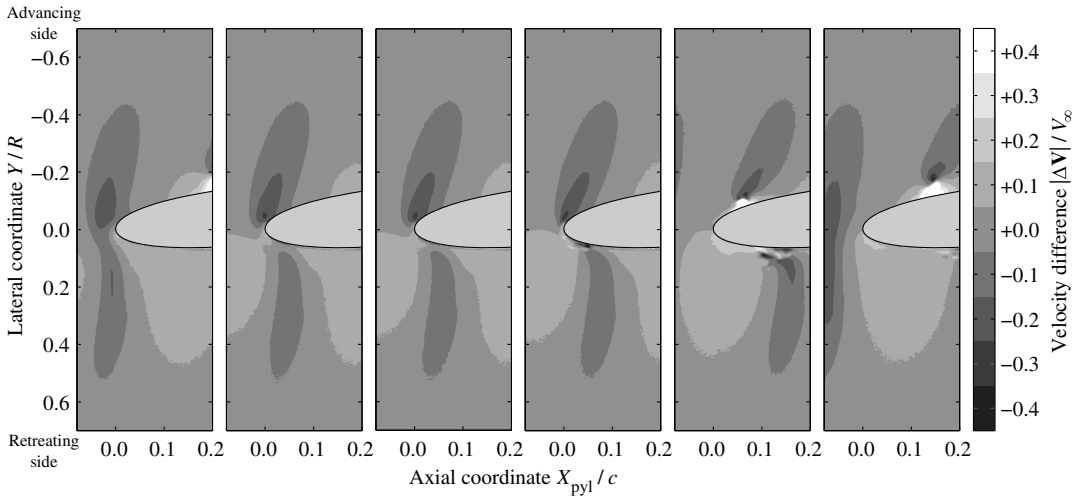

a) ϕ' = –17.5 deg b) ϕ' = –2.5 deg c) ϕ' = 0 deg d) ϕ' = 5 deg e) ϕ' = 27.5 deg f) ϕ' = 52.5 deg

Fig. 17 Vortex-impingement process at the pylon leading edge in asymmetric inflow conditions (velocity difference propeller-on minus propeller-off); $\alpha = 6$ deg, $Z/R = 0.97$.

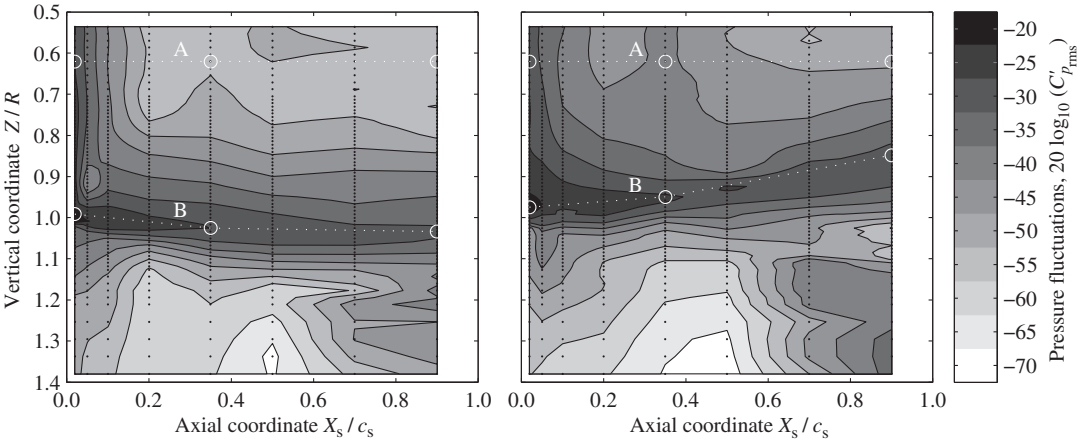

a) Advancing side **b) Retreating side**

Fig. 18 Pressure fluctuations on both sides of the pylon.

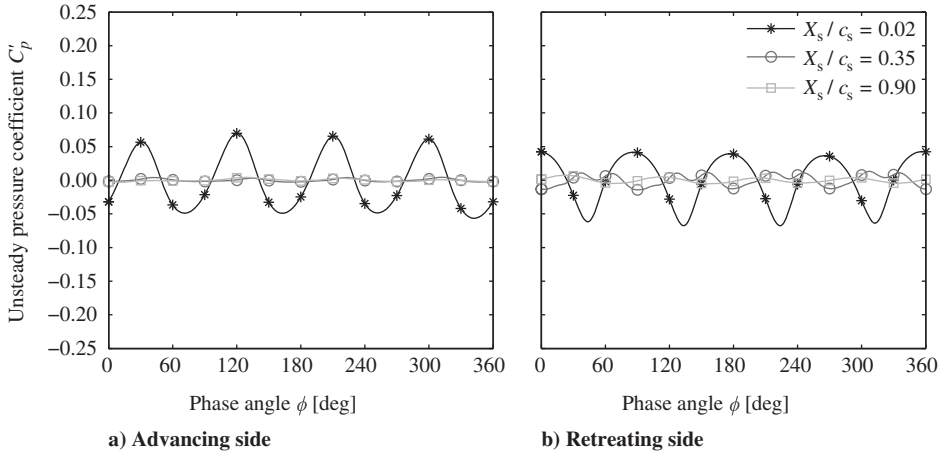

a) Advancing side **b) Retreating side**

Fig. 19 Phase-averaged pressure waveforms in the blade-wake impingement region (line A in Fig. 18, $Z/R = 0.62$).

labeled A and B correspond to the positions for which the pressure waveforms are presented later in Figs. 19 and 20.

Figure 18 shows that the propeller tip vortex is the dominant source of pressure fluctuations on the pylon. Impinging near a vertical coordinate of $Z/R = 1.0$, the tip vortex presents pressure fluctuations with relatively high amplitude over the entire pylon chord. These fluctuations are the result of the blade-tip vortices passing over the microphones. This leads to a periodic pressure

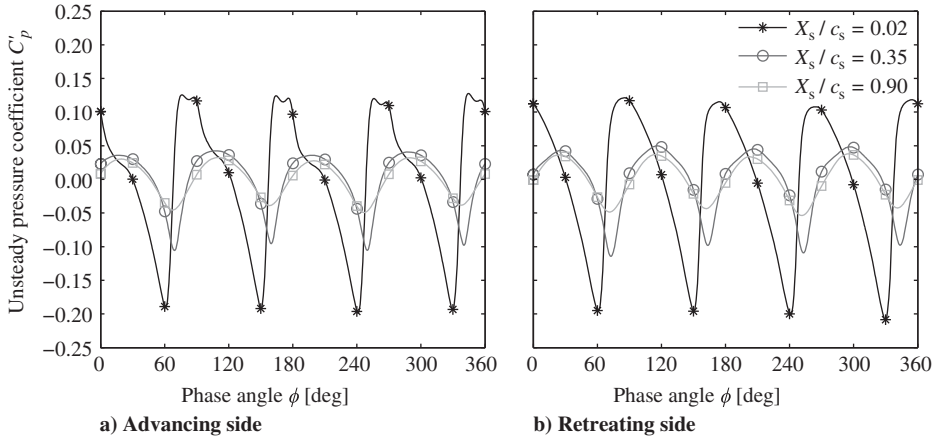

Fig. 20 Phase-averaged pressure waveforms along the tip-vortex trajectory (line B in Fig. 18).

perturbation due to the low pressure in the vortex core. The amplitude of the pressure fluctuations induced by the tip vortex is at a maximum near the pylon leading edge and then slowly decreases along the pylon chord. This was attributed by Johnston and Sullivan [16] to the viscous interaction between the boundary layer and the vortex core, causing a reduction in strength of the part of the vortex immersed in the boundary layer of the pylon. Again, the spanwise displacement of the tip vortices can be seen, confirming the observations made from the PIV data presented in Figs. 11 and 16. Microphone measurements performed at advance ratios different from the baseline value showed that the spanwise displacement increases with decreasing advance ratio. This is due to the increase in swirl and dynamic pressure in the slipstream associated with a decrease in advance ratio, causing increased loading gradients on the pylon. On the other hand, the spanwise displacement of the slipstream edge decreases with increasing angle of attack, as also shown in Fig. 12.

The pressure fluctuations due to the impingement of the blade wakes, inboard of the tip-vortex trajectory, peak at the leading edge of the pylon and then rapidly decrease in the downstream direction. This resembles the response to a gust normal to the airfoil section, caused by the periodic upwash when the blade wakes pass by the pylon. A small region of locally decreased pressure fluctuations can be observed directly inboard of the tip-vortex path near the leading edge on the advancing side (Fig. 18a, $X_s/c_s \approx 0.05$, $Z/R \approx 0.9$). Inspection of the time-accurate pressure data showed that this was due to destructive interference between the pressure perturbations caused by the blade wakes and the tip vortices, as treated in more detail in the discussion of Fig. 20. The opposite situation occurred on the retreating side, leading to a wider region of strong pressure fluctuations on this side of the pylon.

The contours plotted in Fig. 18 only provide information on the rms of the pressure fluctuations on the pylon. To illustrate the associated waveforms, phase-averaged microphone signals and frequency spectra were extracted at the positions of the markers in Fig. 18. Figure 19 provides the waveforms obtained at a spanwise location of $Z/R = 0.62$, corresponding to the response associated with the impingement of the blade wakes (line A in Fig. 18). Both the advancing and retreating sides are included, and three chordwise locations are considered to show the development of the pressure fluctuations in the downstream direction. In a similar way, Fig. 20 provides the waveforms measured along the tip-vortex trajectory (line B in Fig. 18). In this case, the development in the chordwise direction was not considered at constant spanwise coordinate, but instead the path of the tip vortex was followed. The spanwise coordinates at which data were extracted equal $Z/R = [0.992, 1.025, 1.034]$ on the advancing side and $Z/R = [0.975, 0.949, 0.848]$ on the retreating side, for chordwise locations of $X_s/c_s = [0.02, 0.35, 0.90]$, respectively. Spectral analysis was performed on the raw time series using Welch's method [41] with Hann windows, 100 blocks, and no overlap. The corresponding results are plotted for the advancing side in Fig. 21 for the same chordwise and spanwise locations as considered in Figs. 19 and 20. For reference, the spectra acquired outside of the slipstream at $Z/R = 1.38$ are also included. Markers are displayed at multiples of the blade-passage frequency for which the tonal content was at least 3 dB above the broadband noise floor.

The pressure response in the wake-impingement region given in Fig. 19 is clearly periodic and dominated by the component at the blade-passage frequency. This indicates a relatively gradual loading change caused by the wake impingement, which is confirmed by inspection of the spectra shown in Fig. 21. The signals on the retreating and advancing sides have approximately equal amplitude

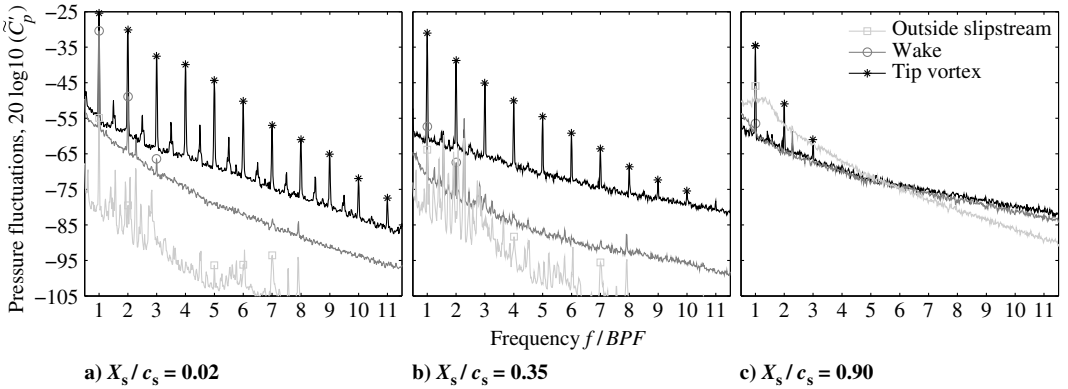

Fig. 21 Frequency spectra of the pressure fluctuations on the advancing side of the pylon outside of the slipstream ($Z/R = 1.38$) and along the blade-wake and tip-vortex impingement trajectories (lines A and B in Fig. 18).

but opposite phase. A negative pressure is induced by the wakes on the retreating side, corresponding to the suction side of the pylon in the current setup. On both sides of the pylon, the pressure fluctuations decrease rapidly in the chordwise direction, as expected based on Fig. 18. On the front part of the pylon (Figs. 21a and 21b), the high turbulence levels in the blade wakes result in increased broadband pressure fluctuations compared to the response outside of the slipstream. Toward the rear of the pylon (Fig. 21c), the broadband levels outside of the slipstream increased significantly due to natural transition. Differences in local inflow angle, velocity, and upstream development of the boundary layer may explain the change in broadband response when compared to that obtained on the part of the pylon immersed in the slipstream.

Figures 20 and 21 show that the amplitude of the pressure fluctuations caused by the tip vortex is larger than that due to the wake impingement. This was also observed in Fig. 18. The passages of the tip-vortex cores are characterized by a strong drop in the pressure. Near the leading edge of the pylon ($X_s/c_s = 0.02$), sharp pressure peaks were obtained (Fig. 20), indicating a richer spectral content of the pressure signal when compared to that resulting from the wake impingement. This is confirmed by the spectra displayed in Fig. 21. The tonal content at the blade-passage frequency and associated multiples clearly dominates the broadband part of the signal, which also increased when compared to the blade-wake impingement region and the part of the pylon outside of the slipstream. The subharmonics, with relatively small amplitude, are most likely measurement artifacts related to slight differences between the propeller blades. Moving downstream, the pressure peaks caused by the impingement of the tip vortex become more sinusoidal-like, and their amplitude decreases. As discussed in relation to Fig. 18, this is due to the viscous interaction between the tip vortex and the pylon boundary layer. Again, the amplitude of the pressure fluctuations is comparable on the advancing and retreating sides. However, the shape of the waveforms differs, with additional secondary oscillations occurring on the advancing side. This is attributed to effects due to the blade wakes, which roll up into the vortex (Fig. 10) and hence also affect the pressure fluctuations measured along the tip-vortex path. This effect was strongest slightly inboard of the trajectory of the tip vortex, explaining the local decrease of the rms of the pressure fluctuations in this region near the leading edge on the advancing side, as highlighted before in the discussion of Fig. 18.

F. Unsteady Loading as a Possible Source of Structure-Borne Noise

The microphone data were used to evaluate the structure-borne-noise indicators defined by Eqs. (1) and (2).

1. *Average Root Mean Square of the Pressure Fluctuations*

The spatial average of the rms of the pressure fluctuations, defined by Eq. (1), was evaluated for the microphone data obtained at each of the operating conditions considered. Figure 22 presents the results as a function of advance ratio (Fig. 22a), propeller–pylon spacing (Fig. 22b), and angle of attack (Fig. 22c). In all subfigures, the operating parameters that were not varied were set equal to their baseline values.

Figure 22a displays the expected decrease in pressure fluctuations with increasing advance ratio. This is due to the reduced strength of the blade wakes and tip vortices associated with the decreased blade loading at higher advance ratio. A nonlinear response is observed, with the pressure fluctuations approaching a nonzero minimum at high advance ratios. Whereas the tip-vortex strength tends to zero when the blades are unloaded, the blade wakes remain. Therefore, nonzero pressure fluctuations are obtained even for the case of an unloaded propeller. In such case, the blade wakes are the dominant source of unsteady pressure on the pylon.

Increasing the propeller–pylon spacing at constant advance ratio results in a reduction of the severity of the incoming flow perturbations due to diffusion of the flow structures in the slipstream. As a result, the pressure fluctuations decrease with increasing axial spacing between the propeller and the pylon (Fig. 22b). The decrease in pressure fluctuations with increasing propeller–pylon spacing is nonlinear because of the nonlinearity in the axial development of the blade-wake and tip-vortex strength. Moreover, at the smallest propeller–pylon spacings, an upstream interaction between the pylon and propeller might have occurred, locally increasing the blade loading, hence aggravating the impingement phenomena. However, this could not be verified using the current measurement setup.

Operating the propeller–pylon setup under asymmetric inflow conditions increases the pressure fluctuations compared to the symmetric case (Fig. 22c). At $\alpha = -6$ deg, the pressure fluctuations increased along the tip-vortex path. At $\alpha = +6$ deg, on the other hand, a separation bubble appeared near the leading edge of the pylon, introducing strong pressure fluctuations at the reattachment point. Finally, at $\alpha = 12$ deg, the suction side of the pylon had stalled in the slipstream region because of the additional upwash caused by the propeller swirl. As a result, the average amplitude of the tonal pressure fluctuations on the suction side of the pylon was decreased in this condition.

2. *Unsteady Lift Coefficient*

The unsteady pylon lift coefficient was calculated using Eq. (2). Figure 23 presents the results as a function of advance ratio (Fig. 23a) and propeller–pylon spacing (Fig. 23b). No sensitivity to the angle of attack could be obtained because the pressure-interpolation procedure does not work if part of the flow on the pylon is separated.

The unsteady lift coefficient of the pylon features a nonmonotonic dependency on the propeller advance ratio (Fig. 23a). This is in contrast with the average amplitude of the pressure fluctuations, which decreased with increasing advance ratio (Fig. 22a). However, a change in advance ratio modifies not only the strength of the blade wakes and tip vortices but also the pitch of the slipstream helix. As a result, the axial separation between the consecutive wakes and tip vortices, and hence the wavelength of the interaction problem, varies with advance ratio. For the four propeller operating conditions considered, the lowest unsteady loads were obtained for advance ratios at which the ratio between the wavelength of the perturbation

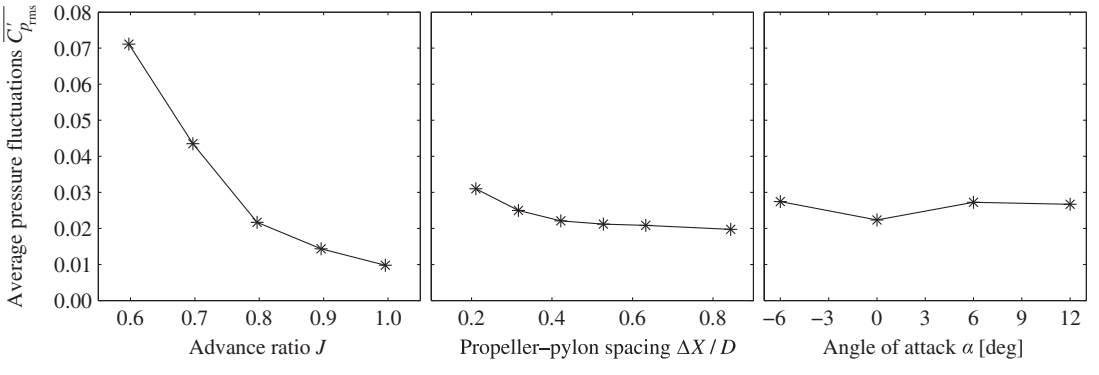

a) $\Delta X / D = 0.42$, $\alpha = 0$ deg **b) $J = 0.8$, $\alpha = 0$ deg** **c) $J = 0.8$, $\Delta X / D = 0.42$**

Fig. 22 Spatial average of the rms of the unsteady pressure coefficient on the pylon vs a) advance ratio, b) propeller–pylon spacing, and c) angle of attack.

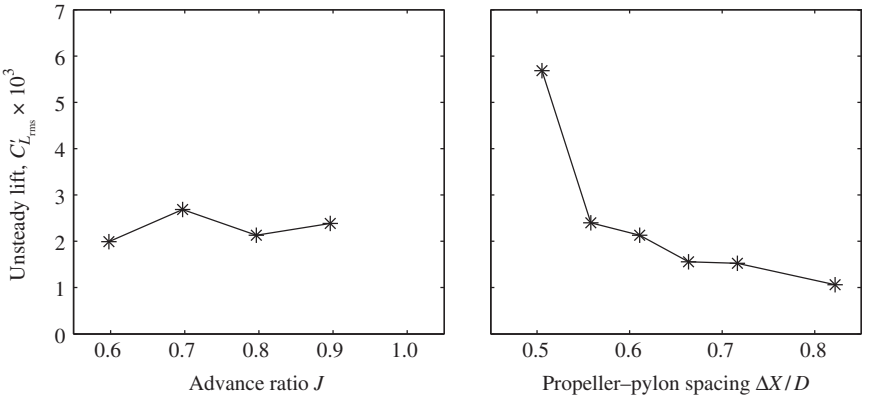

a) $\Delta X / D = 0.42$, $\alpha = 0$ deg **b) $J = 0.8$, $\alpha = 0$ deg**

Fig. 23 Unsteady pylon lift coefficient vs a) advance ratio, and b) propeller–pylon spacing.

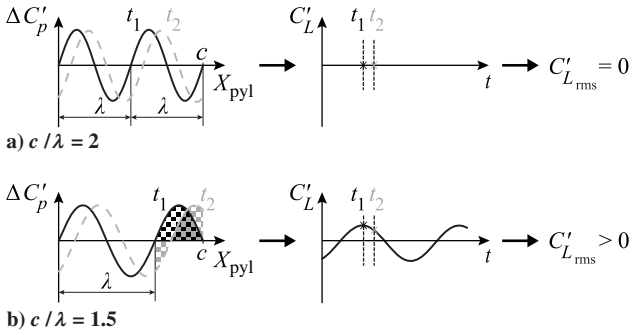

Fig. 24 Illustration of lift coefficient fluctuations for a) integer, and b) noninteger ratios of perturbation wavelength to pylon chord.

associated with the propeller tip vortices and the pylon chord was as close as possible to an integer number. This is explained in Fig. 24, which illustrates the resulting unsteady lift response for a simplified case with two different ratios of perturbation wavelength to pylon chord. In this case, a perfectly sinusoidal pressure perturbation is assumed, which is constant in the spanwise direction. From Eq. (2), it follows that the unsteady lift coefficient on the pylon would be zero for the case of a sinusoidal pressure waveform with wavelength equal to an integer multiple of the pylon chord (Fig. 24a). For noninteger ratios between wavelength and chord, on the other hand, a nonzero unsteady lift coefficient results (Fig. 24b). This implies that structure-borne noise reductions might be obtained by matching the pylon chord with an integer multiple of the axial separation between the propeller tip vortices. In reality, the pressure difference across the pylon will not be perfectly sinusoidal, for example due to differences in the response on the advancing and retreating sides (Fig. 20). Therefore, follow-up experiments involving additional test cases with varying ratios between perturbation wavelength and pylon chord would be required to confirm the applicability of this theory.

In contrast to the sensitivity to the advance ratio, the unsteady lift coefficient monotonically decreases with propeller–pylon spacing (Fig. 23b). In this case, the advance ratio was fixed, and thus the ratio between the wavelength of the pressure disturbance and the pylon chord was constant. Therefore, the relative amplitude of the lift fluctuations was only affected by the relative amplitude of the pressure fluctuations, which feature a decreasing trend with increasing advance ratio as shown in Fig. 22b.

IV. Conclusions

This paper has quantified the unsteady loading caused by the impingement of a propeller slipstream on a downstream pylon. A pylon-mounted tractor-propeller configuration was simulated by positioning a pylon downstream of a sting-mounted propeller in a low-speed wind tunnel. From the measurements taken with an external balance, it was concluded that the installation of the pylon only leads to a minor change of the time-averaged propeller performance. For the current test setup, an increase in thrust of 1% was observed, which was within the repeatability of the measurements.

Particle-image-velocimetry measurements confirmed the presence of the individual blade wakes and tip vortices in the propeller slipstream. The installation of the pylon leads to a spanwise displacement of the propeller slipstream, caused by the spanwise variations in lift on the pylon. The slipstream moves away from the propeller axis on the advancing side and toward the propeller axis on the retreating side. At nonzero angle of attack, the crossflow component over the nacelle modifies the deformation of the slipstream. For an inboard-up rotating propeller, the spanwise displacement of the slipstream is decreased at positive angle of attack and amplified at negative angle of attack.

Measurements of the pressure fluctuations on the pylon using microphones led to the conclusion that the blade-tip vortex dominates the unsteady pressure caused by the impingement of the propeller slipstream. The pressure fluctuations induced by the tip-vortex interaction are periodic with a rich spectral content and persist up to the trailing edge of the pylon. The pressure fluctuations decrease with increasing advance ratio due to the associated reduction in strength of the blade wakes and tip vortices. At high advance ratios, the strength of the tip vortices tends to zero while the blade wakes remain, making the blade wakes the dominant source of unsteady loading in such conditions. Increasing the propeller–pylon spacing reduces the pressure fluctuations due to diffusion of the blade wakes and tip vortices before their interaction with the pylon.

From an assessment of the unsteady loading on the pylon, it is concluded that the unsteady pylon lift displays a nonmonotonic dependency on the propeller advance ratio. In this case, the ratio between the wavelength of the pressure perturbation and the pylon chord is important. The unsteady loading was smallest for cases for which this ratio was closest to an integer value. In an idealized case, for integer ratios, the integrated pressure differential across the pylon is zero. Based on this observation, it is concluded that structure-borne-noise reductions might be obtained by proper tailoring of the pylon chord length.

Acknowledgments

The authors would like to thank Elrick Cornelius and Per Blysa for providing the microphones that were used to perform the unsteady pressure measurements on the pylon surface.

References

[1] Guynn, M. D., Berton, J. J., Haller, W. J., Hendricks, E. S., and Tong, M. T., "Performance and Environmental Assessment of an Advanced Aircraft with Open Rotor Propulsion," NASA TM-2012-217772, Oct. 2012.

[2] Mann, S. A. E., and Stuart, C. A., "Advanced Propulsion Through the 1990s—An Airframer's View," *21st Joint Propulsion Conference*, AIAA Paper 1985-1192, July 1985. doi:10.2514/6.1985-1192

[3] Page, M. A., Ivey, D. M., and Welge, H. R., "Ultra High Bypass Engine Applications to Commercial and Military Aircraft," *SAE Aerospace Technology Conference and Exposition*, SAE International Paper TP-861720, Oct. 1986. doi:10.4271/861720

[4] Goldsmith, I. M., and Bowles, J. V., "Potential Benefits for Propfan Technology on Derivatives of Future Short- to Medium-Range Transport Aircraft," *16th Joint Propulsion Conference*, AIAA Paper 1980-1090, June 1980. doi:10.2514/6.1980-1090

[5] Goldsmith, I. M., "A Study to Define the Research and Technology Requirements for Advanced Turbo/Propfan Transport Aircraft," NASA CR-166138, Feb. 1981.

[6] Block, P. J. W., "Experimental Study of the Effects of Installation on Single- and Counter-Rotation Propeller Noise," NASA TP-2541, April 1986.

[7] Block, P. J. W., and Gentry, G. L., Jr., "Directivity and Trends of Noise Generated by a Propeller in a Wake," NASA TP-2609, Sept. 1986.

[8] Sinnige, T., Ragni, D., Malgoezar, A. M. N., Eitelberg, G., and Veldhuis, L. L. M., "APIAN-INF: An Aerodynamic and Aeroacoustic Investigation of Pylon-Interaction Effects for Pusher Propellers," *CEAS Aeronautical Journal*, 2017. doi:10.1007/s13272-017-0247-2

[9] Magliozzi, B., Brown, P., and Parzych, D., "Acoustic Test and Analysis of a Counterrotating Prop-Fan Model," NASA CR-179590, Oct. 1987.

[10] Eret, P., Kennedy, J., Amoroso, F., Castellini, P., and Bennett, G. J., "Experimental Observations of an Installed-on-Pylon Contra-Rotating Open Rotor with Equal Blade Number in Pusher and Tractor Configuration," *International Journal of Aeroacoustics*, Vol. 15, Nos. 1–2, 2016, pp. 228–249. doi:10.1177/1475472X16642063

[11] Veldhuis, L. L. M., "Propeller Wing Aerodynamic Interference," Ph.D. Thesis, Faculty of Aerospace Engineering, Delft Univ. of Technology, Delft, The Netherlands, 2005.

[12] Witkowski, D. P., Lee, A. K. H., and Sullivan, J. P., "Aerodynamic Interaction Between Propellers and Wings," *Journal of Aircraft*, Vol. 26, No. 9, 1989, pp. 829–836. doi:10.2514/3.45848

[13] Chiaramonte, J. Y., Favier, D., Maresca, C., and Benneceur, S., "Aerodynamic Interaction Study of the Propeller/Wing Under Different Flow Configurations," *Journal of Aircraft*, Vol. 33, No. 1, 1996, pp. 46–53. doi:10.2514/3.46901

[14] Fratello, G., Favier, D., and Maresca, C., "Experimental and Numerical Study of the Propeller/Fixed Wing Interaction," *Journal of Aircraft*, Vol. 28, No. 6, 1991, pp. 365–373. doi:10.2514/3.46036

[15] Ljunggren, S., Samuelsson, I., and Widing, K., "Slipstream-Induced Pressure Fluctuations on a Wing Panel," *Journal of Aircraft*, Vol. 26, No. 10, 1989, pp. 914–919. doi:10.2514/3.45861

[16] Johnston, R. T., and Sullivan, J. P., "Unsteady Wing Surface Pressures in the Wake of a Propeller," *Journal of Aircraft*, Vol. 30, No. 5, 1993, pp. 644–651. doi:10.2514/3.46393

[17] Felli, M., and Falchi, M., "Propeller Tip and Hub Vortex Dynamics in the Interaction with a Rudder," *Experiments in Fluids*, Vol. 51, No. 5, 2011, pp. 1385–1402. doi:10.1007/s00348-011-1162-7

[18] Mukund, R., and Chandan Kumar, A., "Velocity Field Measurements in the Wake of a Propeller Model," *Experiments in Fluids*, Vol. 57, No. 10, 2016. doi:10.1007/s00348-016-2237-2

[19] Miley, S. J., Howard, R. M., and Holmes, B. J., "Wing Laminar Boundary Layer in the Presence of a Propeller Slipstream," *Journal of Aircraft*, Vol. 25, No. 7, 1988, pp. 606–611. doi:10.2514/3.45630

[20] Howard, R. M., and Miley, S. J., "Time-Dependent Boundary-Layer Response in a Propeller Slipstream," *Journal of Aircraft*, Vol. 26, No. 9, 1989, pp. 863–869. doi:10.2514/3.45852

[21] Jonhston, J. F., and Donham, R. E., "Attenuation of Propeller-Related Vibration and Noise," *Journal of Aircraft*, Vol. 19, No. 10, 1982, pp. 858–867. doi:10.2514/3.61568

[22] Miller, B. A., Dittmar, J. H., and Jeracki, R. J., "Propeller Tip Vortex: A Possible Contributor to Aircraft Cabin Noise," *Journal of Aircraft*, Vol. 19, No. 1, 1982, pp. 84–86. doi:10.2514/3.44747

[23] Metcalf, V. L., and Mayes, W. H., "Structureborne Contribution to Interior Noise of Propeller Aircraft," *Business Aircraft Meeting and Exposition*, SAE International Paper TP-830735, Feb. 1983. doi:10.4271/830735

[24] Loeffler, I. J., "Structureborne Noise Control in Advanced Turboprop Aircraft," *25th AIAA Aerospace Sciences Meeting*, AIAA Paper 1987-530, Jan. 1987. doi:10.2514/6.1987-530

[25] Unruh, J. F., "Aircraft Propeller Induced Structure-Borne Noise," NASA CR-4255, Oct. 1989.

[26] Cole, J. E., III, and Martini, K. F., "Structureborne Noise Measurements on a Small Twin-Engine Aircraft," NASA CR-4137, June 1988.

[27] Junger, M. C., Garrelick, J. M., Martinez, R., and Cole, J. E., III, "Analytical Model of the Structureborne Interior Noise Induced by a Propeller Wake," NASA CR-172381, May 1984.

[28] Martinez, R., "Predictions of Unsteady Wing and Pylon Forces Caused by Propeller Installation," NASA CR-178298, May 1987.

[29] Martinez, R., Cole, J. E., III, Martini, K., and Westagard, A., "All-Theoretical Prediction of Cabin Noise due to Impingement of Propeller Vortices on a Wing Structure," *11th Aeroacoustics Conference*, AIAA Paper 1987-2681, Oct. 1987. doi:10.2514/6.1987-2681

[30] Unruh, J. F., "Prediction of Aircraft-Propeller-Induced, Structure-Borne Interior Noise," *Journal of Aircraft*, Vol. 25, No. 8, 1988, pp. 758–764. doi:10.2514/3.45655

[31] Cole, J. E., III, Westagard Stokes, A., Garrelick, J. M., and Martini, K. F., "Analytical Modeling of the Structureborne Noise Path on a Small Twin-Engine Aircraft," NASA CR-4136, June 1988.

[32] Miranda, L. R., and Brennan, J. E., "Aerodynamic Effects of Wingtip-Mounted Propellers and Turbines," *4th Applied Aerodynamics Conference*, AIAA Paper 1986-1802, June 1986. doi:10.2514/6.1986-1802

[33] Snyder, M. H., Jr., and Zumwalt, G. W., "Effects of Wingtip-Mounted Propellers on Wing Lift and Induced Drag," *Journal of Aircraft*, Vol. 6, No. 5, 1969, pp. 392–397. doi:10.2514/3.44076

[34] Scarano, F., and Riethmuller, M. L., "Iterative Multigrid Approach in PIV Image Processing with Discrete Window Offset," *Experiments in Fluids*, Vol. 26, No. 6, 1999, pp. 513–523. doi:10.1007/s003480050318

[35] Romano, G. P., "Analysis of Two-Point Velocity Measurements in Near-Wall Flows," *Experiments in Fluids*, Vol. 20, No. 2, 1995, pp. 68–83. doi:10.1007/BF00189296

[36] Heidelberg, L. J., and Woodward, R. P., "Advanced Turboprop Wing Installation Effects Measured by Unsteady Blade Pressure and Noise," *11th Aeroacoustics Conference*, AIAA Paper 1987-2719, Oct. 1987. doi:10.2514/6.1987-2719

[37] Samuelsson, I., "Experimental Investigation of Low Speed Model Propeller Slipstream Aerodynamic Characteristics Including Flow Field Surveys and Nacelle/Wing Static Pressure Measurements," *Proceedings of the 17th International Congress of the Aeronautical Sciences*, AIAA, Washington, D.C., Sept. 1990, pp. 71–84.

[38] Thom, A. D., "Analysis of Vortex-Lifting Surface Interactions," Ph.D. Thesis, College of Science and Engineering, Univ. of Glasgow, Glasgow, Scotland, U.K., 2011.

[39] Felli, M., Roberto, C., and Guj, G., "Experimental Analysis of the Flow Field Around a Propeller–Rudder Configuration," *Experiments in Fluids*, Vol. 46, No. 1, 2009, pp. 147–164. doi:10.1007/s00348-008-0550-0

[40] Bodstein, G. C. R., George, A. R., and Hui, C.-Y., "The Three-Dimensional Interaction of a Streamwise Vortex with a Large-Chord Lifting Surface: Theory and Experiment," *Journal of Fluid Mechanics*, Vol. 322, Sept. 1996, pp. 51–79. doi:10.1017/S0022112096002704

[41] Welch, P. D., "The Use of Fast Fourier Transform for the Estimation of Power Spectra: A Method Based on Time Averaging over Short, Modified Periodograms," *IEEE Transactions on Audio and Electroacoustics*, Vol. 15, No. 2, 1967, pp. 70–73. doi:10.1109/TAU.1967.1161901